JACS
JOURNAL OF THE AMERICAN CHEMICAL SOCIETY
Article
pubs.acs.org/JACS

Charge Disproportionation in Tetragonal La_2MoO_5, a Small Band Gap Semiconductor Influenced by Direct Mo−Mo Bonding

Diane M. Colabello,[†] Fernando E. Camino,[∥] Ashfia Huq,[§] Mark Hybertsen,[∥] and Peter G. Khalifah*[,†,‡]

[†]Department of Chemistry, Stony Brook University, New York 11794, United States

[‡]Department of Chemistry and [∥]Center for Functional Nanomaterials, Brookhaven National Laboratory, Upton, New York 11793, United States

[§]Spallation Neutron Source, Oak Ridge National Laboratory, Oak Ridge, Tennessee 37830, United States

Supporting Information

ABSTRACT: The structure of the novel compound La_2MoO_5 has been solved from powder X-ray and neutron diffraction data and belongs to the tetragonal space group $P4/m$ (no. 83) with a = 12.6847(3) Å and c = 6.0568(2) Å and with Z = 8. It consists of equal proportions of bioctahedral (Mo_2O_{10}) and square prismatic (Mo_2O_8) dimers, both of which contain direct Mo−Mo bonds and are arranged in 1D chains. The Mo−Mo bond length in the Mo_2O_{10} dimers is 2.684(8) Å, while there are two types of Mo_2O_8 dimers with Mo−Mo bonds lengths of 2.22(2) and 2.28(2) Å. Although the average Mo oxidation state in La_2MoO_5 is 4+, the very different Mo−Mo distances reflect the fact that the Mo_2O_{10} dimers contain only Mo^{5+} (d^1), while the prismatic Mo_2O_8 dimers only contain Mo^{3+} (d^3), a result directly confirmed by density function theory calculations. This is due to the complete disproportionation of Mo^{4+}, a phenomenon which has not previously been observed in solid-state compounds. La_2MoO_5 is diamagnetic, behavior which is not expected for a nonmetallic transition-metal oxide whose cation sites have an odd number of d-electrons. The resistivity displays the Arrhenius-type activated behavior expected for a semiconductor with a band gap of 0.5 eV, exhibiting an unusually small transport gap relative to other diamagnetic oxides. Diffuse reflectance studies indicate that La_2MoO_5 is a rare example of a stable oxide semiconductor with strong infrared absorbance. It is shown that the d-orbital splitting associated with the Mo_2O_8 and Mo_2O_{10} dimeric units can be rationalized using simple molecular orbital bonding concepts.

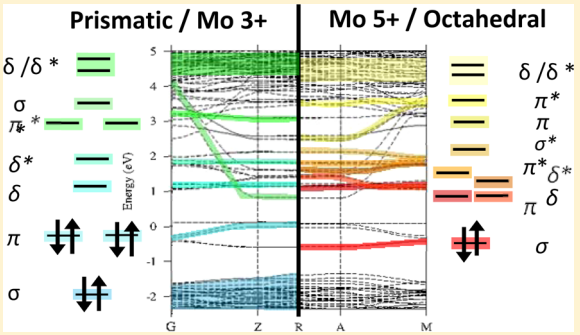

INTRODUCTION

Transition-metal oxides comprise a multifunctional class of materials whose many useful properties are generally derived from the behavior of their d electrons, which can strongly hybridize with oxygen 2p states.[1] While ligand field theory generally provides a good framework for understanding the electronic states of transition metal oxides,[2] we are broadly interested in a special subset of transitional metal oxide compounds which contain direct metal−metal (M−M) bonds that have the potential to introduce radical changes in the electronic structure of oxides that may lead to enhanced functionality. Direct M−M bonds are most commonly found in early 4d and 5d transition metals (with M = Mo, Re, or Ru) that have a small number of electrons in d-orbitals (d^1−d^4). Some examples include the compounds $LnMo_8O_{14}$ (Ln = La, Ce, Pr, Nd, Sm),[3,4] $LnMo_5O_8$ (Ln = La, Ce, Pr, Nd, Sm, Eu, Gd),[5] $Nd_4Re_2O_{11}$,[6] $Ln_4Re_6O_{19}$ (Ln = La, Pr, Nd),[7] and $La_4Ru_6O_{19}$.[8,9] The clearest signature of direct M−M bonds is the short distances between the metal participating in the bonding, as these bond lengths are far shorter than the M−M distances that are typically seen for the same compounds in the absence of M−M bonding (>3 Å). The shortest M−M bond distance reported is a Cr−Cr bond, 1.8028(9) Å, found in a molecular dinuclear chromium diazadiene complex.[10] Other short bond lengths, typically 2.0−2.2 Å, are observed in canonical molecular inorganic compounds with quadruple and quintuple bonds.[11,12] While M−M bonding in molecular compounds has been extensively studied, only handful of solid-state oxide compounds with M−M bonds have been discovered, most of which include the early transition metals Mo or Re. An overview of the electron configuration and experimentally determined bond lengths for solid-state oxides of Mo and Re with dimeric M−M bonding is provided in Table 1. These compounds represent an intriguing interface between the science of molecular compounds and that of extended solids.

The physical properties of compounds with direct M−M bonding can strongly differ from those of conventional oxides with similar electron counts. For example, M−M bonds can suppress paramagnetism in nonmetallic compounds. The compound Ln_2ReO_5 (Ln = Sm, Eu, Gd) contains Re_2O_8 dimers, with Re−Re bonding within the dimer.[23] The average Re oxidation state is 4+, resulting in a d^3 configuration that is

Received: October 31, 2014
Published: December 31, 2014

DOI: 10.1021/ja511218g
J. Am. Chem. Soc. 2015, 137, 1245−1257

Table 1. Some Dimeric M−M (M = Mo, Re) Bonds

compound	ox. state	d^n	M−M (Å)	dimer
$La_4Mo_2O_{11}$ [ref 13]	5+	d^1	2.5905(5)	Mo_2O_{10}
$Y_5Mo_2O_{12}$ [ref 14]	4.5+	$d^{1.5}$	2.496(1)	Mo_2O_{10}
$La_5Mo_4O_{16}$ [ref 15]	4.25+	$d^{1.75}$	2.406(1)	Mo_2O_{10}
$La_2Mo_2O_7$ [ref 16]	4+	d^2	2.478(4)	Mo_2O_{10}
$La_3Re_2O_{10}$ [ref 17]	5.5+	$d^{1.5}$	2.484(1)	Re_2O_{10}
$Nd_4Re_2O_{11}$ [ref 6]	5+	d^2	2.421(1)	Re_2O_{10}
$La_6Re_4O_{18}$ [ref 18]	5+	d^2	2.456(5)	Re_2O_{10}
$Ho_5Re_2O_{12}$ [ref 19]	4.5+	$d^{2.5}$	2.436(2)	Re_2O_{10}
$La_4Re_6O_{19}$ [ref 20]	4.33+	$d^{2.67}$	2.422(7)	Re_2O_{10}
Sm_2ReO_5 [ref 21]	4+	d^3	2.251(1)	Re_2O_8
$La_6Re_4O_{18}$ [ref 18]	4+	d^3	2.235(6)	Re_2O_8
La_2ReO_5 [ref 22]	4+	d^3	2.259(1)	Re_2O_8

generally expected to lead to unpaired electrons and paramagnetism. However, this nonmetallic compound is observed to be diamagnetic. Unusual properties for the metallic members of the general class of compounds with M−M bonding have also been reported. The compound $La_4Ru_6O_{19}$ was the first oxide compound reported to exhibit non-Fermi-liquid behavior, an effect ascribed in part to the exceptionally high density-of-states (very reminiscent of f-electrons) that results from the direct M−M bonding.[8,9] While there have been a number of reports of intriguing properties for compounds with M−M bonds,[17,24,25] a general framework for comprehensively understanding the influence of these bonds on the overall electronic structure remains elusive.

The present work is concerned with the compound La_2MoO_5, which has an average oxidation state of Mo 4+. Another lanthanum molybdate with a 2:1 cation ratio is La_2MoO_6, which contains fully oxidized Mo 6+ cations, and can be readily synthesized in air.[26] This compound has isolated MoO_4 tetrahedra and crystallizes in the tetragonal space group $I4_1/acd$ with a = 5.80 Å and c = 32.04 Å. There have been a few prior reports of reduced compounds with the general composition of Ln_2MO_5 (Ln = La, Y, Ce−Lu; M = Mo, Re), though most of these studies were carried out decades ago.[27−31] The original report of Ln_2MO_5 phases with the α-Nd_2ReO_5 structure type suggested a body-centered tetragonal cell with a = 8.81 Å and c = 5.89 Å for Nd_2ReO_5. The atomic arrangement of this structure type remained unknown until the growth of crystals allowed the structure of La_2ReO_5 to be solved using single crystal X-ray diffraction (XRD) techniques.[22,32] In prior work, this lanthanum compound was referred to as $La_4[Re_2]$-O_{10} to emphasize the Re_2O_8 square planar dimers in this structure. Later, other types of molybdate Ln_2MoO_5 compounds were also discovered.[30,31] These compounds were either reported in a cubic fluorite-type unit cell ($a \sim 5.7$ Å)[33] or in a more complex monoclinic unit cell which has curiously been ascribed to both Ln_2MoO_5 and $Ln_5Mo_2O_{12}$ compositions.[14,34] A recent investigation of the fluorite-related structure type by powder neutron diffraction and thermogravimetric analysis found a variable stoichiometry ranging from $Ln_2MoO_{4.8}$ to $Ln_2MoO_{5.2}$, with good oxygen anion conductivity at elevated temperatures resulting from the abundant oxygen vacancies relative to the ideal fluorite composition of Ln_2MoO_6.

In the present work, a novel polymorph of La_2MoO_5 is reported and its structure has been solved from powder diffraction data. This compound is demonstrated to adopt a new structure type which is crystallographically related to that of tetragonal La_2ReO_5. The physical properties of this compound have been measured, and are unexpected for a compound whose average Mo oxidation state is 4+. The band gap of this compound is much smaller than for other semiconducting molybdates, resulting in the substantial absorption of infrared light. Density function theory (DFT) studies have been carried out to understand the role of metal−metal bonding in determining both the novel structure type and the unexpected physical properties, and the observed physical properties of this phase can be readily understood in terms of its electronic structure. It is shown that the DFT-calculated energy levels can be simply rationalized in terms of bonding and antibonding orbitals generated through a molecular-orbital analysis of the dimeric units in La_2MoO_5.

EXPERIMENTAL SECTION

La_2O_3 (99.99%, Alpha Aesar) and MoO_3 (99.95%, Alpha Aesar) were used as starting materials, with La_2O_3 dried at 900 °C for several hours before being weighed to eliminate absorbed moisture. La_2MoO_6 was prepared by grinding stoichiometric amounts of the starting materials using an agate mortar and pestle. This powder was then placed in a dense alumina crucible (CoorsTek) and reacted in air in a box furnace at 950 °C for about 12 h. La_2MoO_5 was synthesized by heating a ∼1 g 1/2 in. pellet of La_2MoO_6 in a 1 in. ID quartz tube under a flowing gas mixture of 5% H_2/95% N_2 (60 mL/min, passed through a line drier) in a Lindberg/BlueM Mini-Mite furnace at temperatures of 900−950 °C for about 3 days with intermediate grinding. Upon completion of the reaction, the powder was slate gray in color.

Laboratory XRD data were collected using a Bruker D8 Advance diffractometer with a nickel-filtered Cu K_α source. Data were collected over a 2θ scan range of 7−140° using a step size of 0.02°, a fixed divergence slit of 0.3°, and Soller slit widths of 2.5°. Synchrotron XRD were collected at the APS 11-BM beamline. Powder samples were packed into 0.8 mm Kapton capillaries. A wavelength of 0.41333 Å was used to collect data over a 2θ scan range of 1−50° using a step size of 0.001°. Time of flight (TOF) neutron powder diffraction measurements were collected at both 12 and 300 K on the POWGEN beamline located at the Spallation Neutron Source (SNS) of Oak Ridge National Laboratory during run cycle 2013A. Samples, approximately 2 g in mass, were loaded into an 8 mm diameter vanadium can which was placed in the FERNS cryogenic sample changer. Data were collected using a repetition rate of 60 Hz in frame 1.5, corresponding to a d-spacing range of 0.28−3.09 Å, with a total proton charge of 3.6 to 7.2 × 10^{12} (1−3 h collection time). All diffraction data were analyzed using the TOPAS software package (V4.2, Bruker AXS).

Magnetic susceptibility measurements were done in a Quantum Design Physical Property Measurement System (PPMS) using a vibrating sample magnetometer (VSM) attachment. The magnetic response was measured over the temperature range of 2−350 K with applied magnetic fields of 1000, 10,000, and 50,000 Oe. Both field-cooled (FC) and zero-field-cooled (ZFC) sweeps were conducted.

Optical absorbance measurements were done using a two-beam PerkinElmer Lambda 950 UV−vis/NIR spectrometer with a 60 mm diameter Spectralon-coated integrating sphere to collect diffuse reflectance data. Undiluted samples were packed about 10 mm deep into black metal sample holders with a 1.5 mm thick quartz window (16.60 mm in diameter). Ground $BaSO_4$ powder (Alfa Aesar 99.99%) was used as a 100% reflectance standard. The Kubelka−Munk transform was used to calculate relative absorbances from the reflectance data through the relationship $\alpha_{KM} = \alpha/s = (1 - R)^2/(2R)$, where α_{KM} is a relative absorbance, α is the absolute absorbance, s is an generally unknown scattering coefficient, and R is the reflectance measured in the spectrometer.

Four-probe resistivity measurements were carried out on bar-shaped samples cut from a sintered 1/2 in. diameter pellet. The most distant ends of the bar were coated with silver epoxy (EPOTEK, H20E) to provide the current contacts, while voltage was measured on two in-line point contacts on the top of the sample. A custom sapphire stage

DOI: 10.1021/ja511218g
J. Am. Chem. Soc. 2015, 137, 1245−1257

with Cu pads was used to support the sample during measurements. Pt wires (0.025 mm) were used to connect the sample to the stage with contacts made using silver epoxy, while metal-to-metal pressure contacts connected the stage to external cables leading to the Kiethley 2636 source meter used to control the resistivity measurements (which were typically done at an applied voltage of about 25 V). The sample stage was mounted inside a controlled-atmosphere rapid-thermal-annealing chamber (MBE Komponenten GmbH) in which an inert Ar atmosphere was maintained. A typical sweep was performed by first stabilizing the sample temperature at 30 °C for several minutes, ramping up to 300 °C in 30 min, holding for 10 min, and finally ramping down to 30 °C at the same rate.

Thermogravimetric analysis (TGA) was used to determine the Mo oxidation state in La_2MoO_5 using a TA Instruments Q5000 IR instrument. A powder sample (10−20 mg) was heated in a 100 μL alumina pan under flowing O_2 (25 mL/min) with a continuous ramp rate of 1 °C/min during both heating and cooling, and with additional holds at 150 °C (2.5 h) and 950 °C (4 h). In order to minimize errors due to buoyancy and surface-adsorbed moisture, the mass change was determined by comparing the sample mass at 150 °C before and after cooling.

DFT calculations using the linear muffin tin orbital (LMTO) 47c code were carried out in order to obtain an understanding of the metal−metal bonding through a "fatbands" analysis of orbital contributions.[35] The program uses a LMTO approach within a tight-binding approximation and an atomic sphere approximation to model voids within the unit cell using empty spheres. Lattice parameters and atomic positions taken from Rietveld refinement results were used as input for the calculations and integration over k space was performed with a 6 × 6 × 12 grid of 77 irreducible k points.

Further DFT calculations were performed with the projector augmented wave method[36] as implemented in the VASP code[37,38] using the local density approximation (LDA)[39,40] and with the LDA +U method.[41] For the latter, the U and J parameters were applied to the Mo d-states with values 3.0 and 0.3 eV.[42] Initial lattice parameters and atomic positions were taken from the experimental structural refinement. Electronic and optical characteristics were calculated following internal relaxation of the atomic positions with lattice parameters held fixed. Structural properties were assessed by performing total energy calculations for a series of cell volumes over a range from approximately −24% to +12% relative to the measured cell volume while allowing the c/a ratio and internal coordinates to relax at each point. Final cell parameters were determined by a fit to the Murnaghan equation of state.[43]

RESULTS AND DISCUSSION

In the course of materials discovery efforts within the La−Mo−O phase space, it was discovered that the high temperature reduction of the precursor phase La_2MoO_6 resulted in the formation of a novel reduced lanthanum molybdate. The powder XRD pattern for this new phase (Figure 1) could not be indexed using the cell parameters previously reported for known phases such as cubic or monoclinic La_2MoO_5 but was found to closely resemble the XRD pattern of tetragonal La_2ReO_5, which crystallizes in the tetragonal space group $I4/m$ (no. 87) with unit cell dimensions of a = 8.935 Å and c = 6.011 Å. As illustrated in Figure 1, this La_2ReO_5 structure contains isolated Re_2O_8 square prisms which have very short Re−Re bond lengths of 2.26 Å, reflecting the strong metal−metal bonding in this phase.[22]

All of the major diffraction peaks in the lanthanum molybdate diffraction pattern could be well modeled in both Le Bail and Rietveld fits using the analogous La_2ReO_5 structural model as a starting point, suggesting that the stoichiometry of this novel phase is La_2MoO_5. The refined molybdate lattice parameters using this $I4/m$ structural model were a = 8.958 Å and c = 6.051 Å, with additional crystallographic parameters

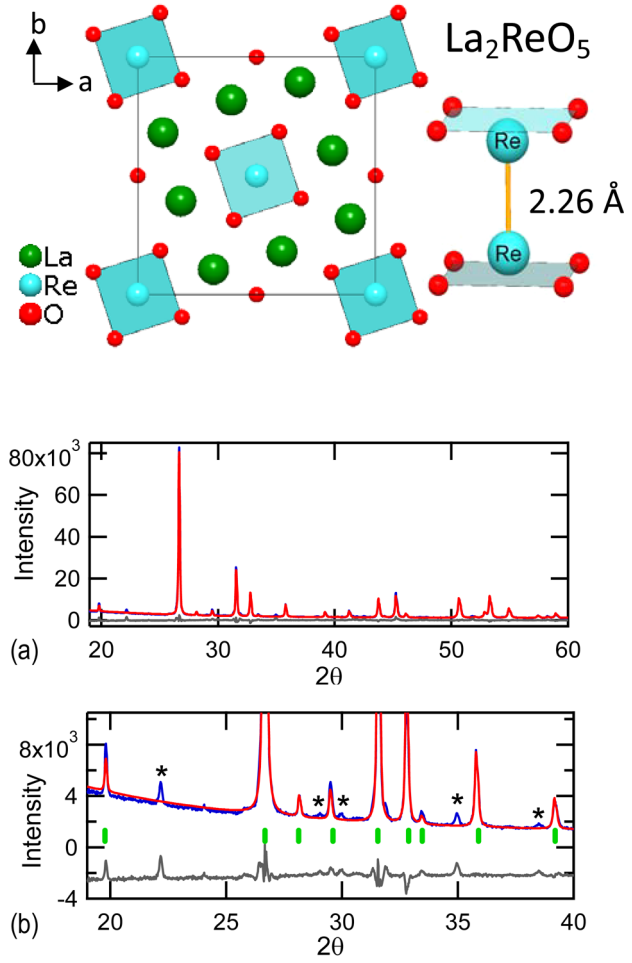

Figure 1. Top: Structure of La_2ReO_5, with an isolated dimeric Re_2O_8 square prism also shown to illustrate the short Re−Re bond distances. Bottom: Two different views of the Rietveld refinement of laboratory powder XRD data for La_2MoO_5 using the La_2ReO_5 ($I4/m$) approximant structural model, with refined lattice parameters of a = 8.96 Å and c = 6.05 Å. Data are shown in blue, the modeled intensities in red, the difference pattern in gray, and the predicted reflection positions in green. The fit is very good in most aspects but misses a series of weak peaks (*) that can be fit in the true $\sqrt{2} \times \sqrt{2} \times 1$ superstructure ($P4/m$).

given in Table S1. However, there are some subtle indications that this proposed structure is incorrect. While an R_{wp} of 5.37 can be achieved through a Le Bail fit, the best Rietveld fit with this model gave an R_{wp} of 6.98, suggesting that peak intensities were not optimally modeled. A close look at long scans collected in a laboratory X-ray diffractometer with good signal-to-noise ratios indicated the reproducible presence of additional weak peaks (marked with asterisks) that cannot be indexed using the La_2ReO_5-type structural model or by plausible impurity phases, a result which was confirmed in follow-up high-resolution synchrotron diffraction studies with reduced peak widths and improved signal-to-noise ratios. These peaks could, however, be fit with a $\sqrt{2} \times \sqrt{2} \times 1$ superstructure of the $I4/m$ symmetry cell. Furthermore, when the Mo valence was calculated from the Mo−O bond distances in this La_2MoO_5 structural model using bond valence sum methods, the resulting Mo valence of +3.15 was not consistent with the expected stoichiometry.

DOI: 10.1021/ja511218g
J. Am. Chem. Soc. 2015, 137, 1245−1257

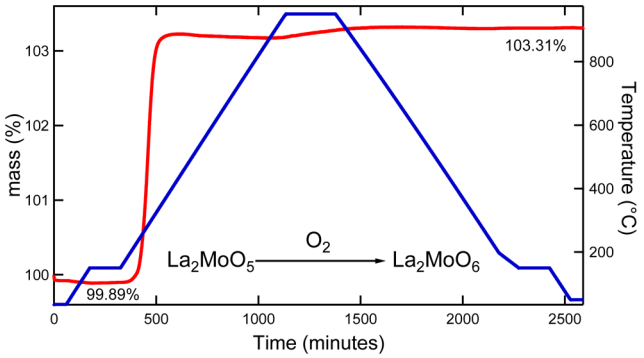

Figure 2. TGA data showing the mass changes (red) as La_2MoO_5 is thermally oxidized to La_2MoO_6 over the programmed temperature profile (blue). The sample % mass at 150 °C before and oxidation is indicated.

TGA oxidation experiments (Figure 2) were used to directly probe the oxidation state of Mo and to thereby probe the composition of this phase. The mass gain during oxidation was calculated from the difference in masses during extended holds at 150 °C before and after thermal oxidation to eliminate potential errors from both buoyancy and from surface-adsorbed water. The final product after oxidation at 950 °C was found by XRD (Figure S1, Table S2) to consist of single phase La_2MoO_6, confirming that there was no cation volatility during the original synthesis or during the subsequent TGA oxidation experiments. The observed mass change (3.53%) is in good agreement with the expected mass change (3.42%) for a sample with the stoichiometry La_2MoO_5 and a 4+ average Mo oxidation state.

With this basic knowledge, structure determination was then attempted. Charge flipping methods were used to first assign the heavy atom (La and Mo) positions using synchrotron XRD data. Peaks positions and intensities from a Le Bail fit were used as input, and trial calculations were performed both with and without symmetry constraints. The SUPERFLIP symmetry analysis indicated that the highest of the three possible space group symmetries consistent with the diffraction data ($P4/m$) was preferred, and this space group was used throughout the remainder of the structure solution process.[44] It was found that the heavy atom positions in La_2MoO_5 were essentially unchanged relative to the La_2ReO_5-type subcell. Next, oxygen positions were determined from neutron data and Fourier difference maps. All atomic sites were found to be fully occupied. The final structure refinements were carried out using only neutron diffraction data (which provided good sensitivity to all atoms) in space group $P4/m$, since the lower symmetry space groups ($P4$ and $P\bar{4}$) with the same systematic absence conditions were found to produce negligible improvements in the refinement quality while exhibiting substantially increased statistical uncertainties in atom positions, reflecting the correlation effects that occur when symmetry-equivalent atoms are independently refined. The final refinement results are presented in Table 2, while selected bond distances are given in Tables 3 (for Mo) and S3 (for La). Similar quality fits were also obtained using synchrotron diffraction data (Table S4), and the refined synchrotron lattice parameters of a = 12.66871(6) and c = 6.05048(3) are expected to be more accurate than those of the neutron diffraction data due to the parallel beam and fixed diffractometer geometry used in the synchrotron data collection.

Table 3. Mo−O and Mo−Mo Bond Distances

atom 1	atom 2	mult	distance (Å)
Mo1	O2	× 4	2.010(6)
	Mo1 (short)	× 1	2.22(2)
	Mo1 (long)	× 1	3.83(1)
Mo2	O1	× 4	1.994(5)
	Mo2 (short)	× 1	2.28(2)
	Mo2 (long)	× 1	3.78(1)
Mo3	O4	× 2	1.866(5)
	O5	× 2	2.000(6)
	O6	× 2	2.135(5)
	Mo3(short)	× 1	2.684(8)
	Mo3(long)	× 1	3.369(6)

The final refined structure of La_2MoO_5 is shown in Figure 3. Although the arrangement of heavy atoms (La, Mo) is essentially the same as in the La_2ReO_5 structure, a set of new Mo coordination environments are observed due to some oxygens in the superstructure moving to significantly different positions (~1.5 Å away from the analogous positions in La_2ReO_5) in the superstructure. This results in La_2MoO_5 having two different types of coordination polyhedra (Mo_2O_8 square prisms and Mo_2O_{10} edge-sharing bioctahedra, present in equal amounts), in contrast to La_2ReO_5, which has only Re_2O_8 prisms. The alternating pattern of these two building blocks gives rise to the $\sqrt{2} \times \sqrt{2}$ superstructure of La_2MoO_5.

While there are only two different types of Mo bonding environments, there are three different crystallographic Mo

Table 2. La_2MoO_5 Crystallographic Parameters and Atomic Sites ($P4/m$)

		atom	Wykoff	x	y	z	B_{eq}
crystal system	tetragonal	La1	4j	0.2041(4)	0.1093(4)	0	0.73(8)
space group	$P4/m$ (no. 83)	La2	4j	0.3005(4)	0.3901(4)	0	0.39(6)
Z	8	La3	4k	0.2719(4)	−0.0961(4)	1/2	0.51(6)
radiation	neutron (TOF)	La4	4k	0.3871(4)	0.2220(4)	1/2	0.51(5)
temperature	300 K	Mo1	2g	0	0	0.316(2)	0.55(9)
λ (Å)	1.066 (center)	Mo2	2h	1/2	1/2	0.312(2)	0.44(8)
range of collection	$0.28 < d < 3.09$	Mo3	4i	0	1/2	0.2217(7)	0.51(4)
lattice parameters (Å)	a = 12.6684(4)	O1	8l	0.3518(4)	0.5417(4)	0.7561(6)	0.58(5)
	c = 6.0526(2)	O2	8l	−0.0433(5)	0.8533(4)	0.7711(5)	0.76(7)
cell volume (Å^3)	971.37(7)	O3	8l	0.2546(4)	0.7555(4)	0.2532(5)	0.59(4)
ρ_{calc} (g/cm^3)	6.2054(5)	O4	8l	0.0497(4)	0.6378(4)	0.2528(5)	0.93(6)
R_{bragg}	2.48	O5	4j	0.4616(5)	0.8894(5)	0	0.73(7)
R_{wp}	3.39	O6	4k	0.4655(6)	−0.0976(5)	1/2	0.74(7)

DOI: 10.1021/ja511218g
J. Am. Chem. Soc. 2015, 137, 1245−1257

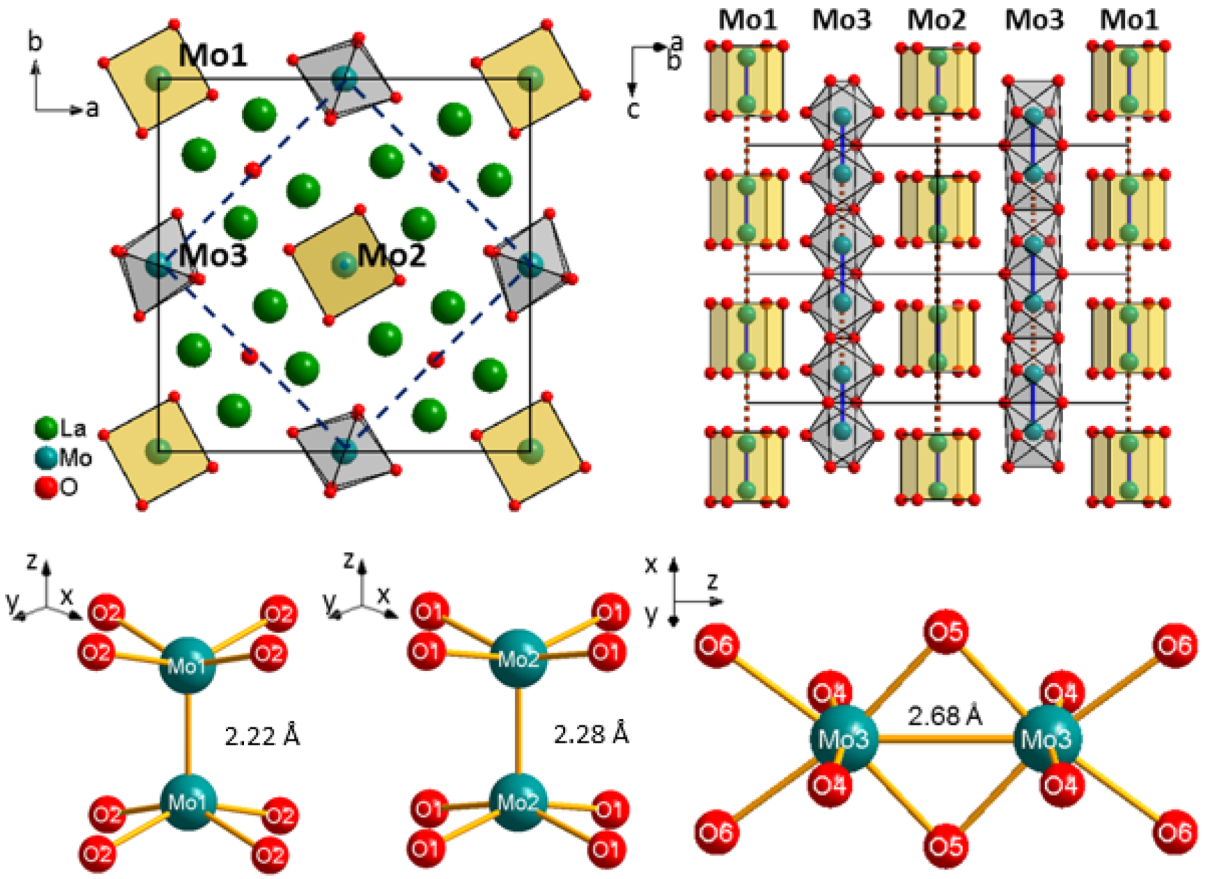

Figure 3. Top left: The tetragonal $P4/m$ La_2MoO_5 unit cell is displayed with the boundary of the $I4/m$ subcell of La_2ReO_5 (dashed lines) superimposed. Top right: Chains of Mo_2O_8 (Mo1 and Mo2 site) and Mo_2O_{10} (Mo3 site) dimers in La_2MoO_5 are shown with Mo−Mo bonds drawn with solid blue lines and nonbonding Mo−Mo neighbors connected with dashed orange lines. Bottom: Local geometry of the three Mo sites and the nonstandard coordinate axes used to define their d-orbitals.

sites. The Mo1 and Mo2 sites sit at the 2g and 2h Wykoff positions which both have four-fold rotational symmetry along the Mo−Mo bond axis, resulting in perfectly square arrangements of oxygens around these square prismatic sites. These two sites are found in separate Mo_2O_8 dimers with Mo−Mo bond lengths of 2.22(2) and 2.28(2) Å, respectively. The Mo3 site (4i Wykoff position) has a lower two-fold rotational symmetry, as four-fold rotational symmetry is not compatible with the formation of the octahedra in these edge-sharing bioctahedral Mo_2O_{10} dimers. These octahedral dimers have much longer Mo−Mo bond lengths of 2.684(8) Å, an indication that the Mo−Mo bond order is reduced in the Mo_2O_{10} octahedral dimers relative to the Mo_2O_8 prismatic dimers. Since all of the Mo−Mo bonds in both the octahedra and in the square prisms are oriented parallel to the c-axis, the structure can be considered to have chains of both types of polyhedral units running parallel to the c-axis, as illustrated in Figure 3. The sum of the Mo−Mo bond length and the nonbonded Mo−Mo distance is necessarily equal to the c-axis length for both the prismatic and octahedral chains.

The two crystallographically distinct types of Mo_2O_8 square prisms both have a single type of Mo−O bond length due to the four-fold symmetry of the structure, and this length is ∼2.00 Å for each site. In contrast, the Mo_2O_{10} octahedral dimers have a wider distribution of Mo−O bond lengths (1.87, 2.00, and 2.13 Å) that may either be indicative of a second-order Jahn−Teller distortion[45] of the central Mo cation or might just reflect the symmetry breaking caused by the alternating short and long Mo−Mo distances in the octahedral chains. An additional important building block within the La_2MoO_5 structure is the OLa_4 tetrahedra, which have an O3 site at their center. The bond distances within OLa_4 tetrahedra are in general known to be shorter than typical O−La bonds, and indeed short bond distances of ∼2.4 Å are found for these tetrahedra. If La cations are drawn at the center of coordination polyhedra, environments of distorted LaO_8 cubes or LaO_7 monocapped trigonal prisms are observed. The bond distances in these polyhedra are generally short (2.4−2.7 Å).

It is well established that the experimentally determined bond lengths can be utilized to obtain reasonable estimates of ion valences through the bond valence sum method.[46−48] The contribution of each individual bond to the total valence of a Mo cation can be obtained through the relationship: $v_i = e^{(R_0 - R_i)/b}$, where the valence contribution from the i^{th} ligand can be calculated from its bond distance, R_i, based on two parameters R_0 and b for which tabulated values are typically available based on empirical analyses of the prior crystallographic literature. The experimental bond distances (R_i) for La_2MoO_5 were determined through Rietveld refinement of neutron powder diffraction data (Table 3). The best choice of R_0 and b is not clear since these parameters are often valence-specific, and the thus the choice of an expected valence will affect the valence calculated using BVS methods. When a variety of BVS parameters suggested for Mo cations are investigated (Tables S5 and S6), it is robustly found that there is a very large difference (1.5−2 valence units, v.u.) in the

DOI: 10.1021/ja511218g
J. Am. Chem. Soc. 2015, 137, 1245−1257

valence predicted for the prismatic and octahedral sites. This suggests that charge disproportion is occurring, with the expected Mo valence of 4+ not observed for any site. Instead, the prismatic sites are found to have Mo 3+ (d^3), while the octahedral sites have Mo 5+ (d^1). Final valences (Table 4) were

Table 4. Bond Valence Sum Analysis

Mo site	O site	bond length	site type	valence/bond	valence/site
Mo1	O2	2.010	prism	0.62	2.49
Mo2	O1	1.994	prism	0.65	2.59
Mo3	O4	1.866	Oct	1.03	4.51
	O5	2.000	Oct	0.72	
	O6	2.135	Oct	0.50	

therefore calculated using Mo 3+ BVS parameters for the prismatic sites and Mo 5+ BVS parameters for the octahedral site (Mo3), and the difference in valence between the two sites when calculated in this manner was 2.0, a value which suggests complete disproportionation. This represents the first example of the disproportionation of Mo^{4+} within any solid-state structure.

The bond valence sum analysis also highlights another unusual aspect of bonding within this system. The calculated valence for all three of the Mo sites is reduced relative to the formal oxidation state by about 0.5 valence units. This is a very large and systematic difference that indicates significant variations in the observed Mo−O bond lengths relative to those generally expected for other compounds with the same Mo oxidation state and coordination number. The BVS parameters can also be used for the reverse process of predicting what the average bond length should be for a given valence (Tables S7−S9), and it can be seen from this analysis that the Mo−O bonds in La_2MoO_5 are about ∼0.05 Å longer than would normally be expected based on their oxidation state (Table 5). This demonstrates that the presence

Table 5. Refined vs Ideal Mo−O Bond Lengths (Å)

	refined distance	ideal distance (BVS)	Δ(distance)
Mo1	2.01	1.94−1.97	+0.04−0.06
Mo2	1.99	1.94−1.97	+0.02−0.05
Mo3	2.00	1.94−1.95	+0.05−0.06

of metal−metal bonding results in a substantial weakening of Mo−O bonds within these dimeric units relative to expectations for isolated polyhedra. Metal−metal bonding therefore offers the opportunity to tune bond strength in a manner that may be useful for applications such as catalysis, where performance in many cases directly correlates with bond strength.

Although disproportion of ions in the solid state is uncommon, it is in many cases associated with intriguing functionality. We first note that even though the change in oxidation state is often referred to as "charge disproportionation", the term "charge" is very misleading as changes in oxidation state need not be accompanied by changes in the electrostatic charge associated with ions,[49,50] as has been very effectively demonstrated in some recent theoretical investigations.[51] Instead, disproportionation refers to a change in the integer "formal charge" of ions, which is more commonly called an oxidation state, and thus should be thought of as "formal charge disproportionation". The oxidation state of ions is often the same as their valence state (which corresponds to the number of orbitals involved in chemical bonding), though this need not be the case as has been described in a recent overview.[49] The real charge of ions can only be clearly assigned integer values for isolated gas phase ions, and as such, it is not sensible to think of solid-state compounds in terms of integer charges.

Typically, disproportionation is driven by an energetic impetus to satisfy Hund's rule, which specify that closed shell electron configurations are particularly stable and that half-filled shells are next most stable. The energetic advantages conferred by achieving a closed shell are clearly seen in the stable valences of many p-block cations, such as Bi^{5+}/Bi^{3+}, Pb^{4+}/Pb^{2+}, Tl^{3+}/Tl^{+}, Sb^{5+}/Sb^{3+}, and Sn^{4+}/Sn^{2+}. These valence states can coexist in a single compound, as exemplified by the compound Sb_2O_4 which contains only Sb^{3+} and Sb^{5+}, which can be considered to be an example of disproportionation since the average Sb oxidation state is 4+.[52] Sb_2O_4 is therefore necessarily an example of a mixed valence compound in which different valences states of the same element coexist in a compound. Interestingly, it has been reported that the intermediate 4+ oxidation state of Sb and Bi can be stabilized by dilution,[49] and it has been hypothesized that the strong tendency of electrons in the nominal 4+ state of these ions to disproportionate leads to a tendency for electrons to pair in a manner that facilitates the superconductivity at temperatures up to 30 K in perovskite compounds such as $Ba(Pb_{0.75}Bi_{0.25})O_3$ (T_c ∼ 12 K),[53] $Ba_{0.6}K_{0.4}BiO_3$ (T_c ∼ 30 K),[54] as and $Ba(Pb_{0.75}Sb_{0.25})O_3$ (T_c ∼ 3 K).[55] There has been resurgent interest in halide analogues of this system[56] due to the prediction of superconductivity at about 20 and 30 K for $CsTlCl_3$ and $CsTlF_3$, respectively.[57]

Unlike the p-block elements, disproportionation in transition metals can be driven by the electron configuration rearranging so that the resulting electronic states are either half-filled or completely filled (or a combination of these two cases for the two different valences that result from disproportionation). The electron configurations which lead to disproportionation will vary with the local geometry of the transition metal due to the different degrees to which ligand field effects can lift the native five-fold degeneracy of d-orbitals expected for an isolated atom and are of course affected by the spin state (high spin/low spin) of the cation as well. Thus, the tendency of the high spin octahedral d^4 configuration to disproportionate drives both the $2\ Fe^{4+} \rightarrow Fe^{3+} + Fe^{5+}$ speciation in the unusual solid-state compound $CaFeO_3$[58] as well as the well-known instability of Mn^{3+} ions in aqueous solution, which is relevant to the modern design of oxygen evolution reaction (OER) electrocatalysts.[59] Disproportionation is also known to occur for octahedral d^7 ions, resulting in the $2\ Ni^{3+} \rightarrow Ni^{2+} + Ni^{4+}$ speciation in perovskites such as $NdNiO_3$.[60] While octahedral disproportionation examples are probably most common due to the predominance of this coordination environment, disproportionation can occur in nonoctahedral geometries such as the trigonal prismatic d^6 Co^{3+} sites in $Sr_5Co_4O_{15}$.[61] Although examples for the later 4d and 5d transition metals are less common than for the 3d transition metals described above, examples such as AgO[49] and $CsAuCl_3$[62] are known.

While Hund's rule typically provides the driving force for transitions between integer valence states, similar speciation processes have been reported for transition metals in noninteger valence states, such as the $2\ Fe^{2.5+} \rightarrow Fe^{2+} + Fe^{3+}$ speciation reported for Fe_2BO_4[63−65] and the $2\ Ir^{3.5+} \rightarrow Ir^{3+} + Ir^{4+}$ speciation reported for $CuIr_2S_4$,[66,67] and of course the

DOI: 10.1021/ja511218g
J. Am. Chem. Soc. 2015, 137, 1245−1257

classic Verwey transition of Fe_3O_4 whose precise nature has been much debated.[68−70] Such compounds are often said to be "charge ordered", though of course the same qualifiers on the use of the term charge apply. These compounds do not represent the disproportionation of ions (as the ground state of an atom does not have a half-integer number of electrons). These speciation reactions are better considered to be an example of a thermally driven transition between a mixed valence state (where electrons are localized on one ion) and an intermediate valence state (where electrons are delocalized over multiple ions), with the former state being enthalpically favored and the latter being entropically favored. As such, these transitions are perhaps better thought of as the "charge disordering" of the native mixed valence ground state.

In this context, the compound La_2MoO_5 is a particularly interesting example of charge disproportionation given the scarcity of other examples among the early 4d and 5d transition metals. Furthermore, even though the Mo^{3+} and Mo^{5+} sites that result from disproportionation could be equivalent in a hypothetical compound in which all Mo cations possessed the average 4+ state (as is the case for the Re^{4+} cations in the closely related structure of La_2ReO_5), the coordination of the two Mo cations in disproportionated La_2MoO_5 is completely different as these cations are either square planar (CN 4) or octahedral (CN 6) in their local geometrical environment even though the stoichiometric ratio of Mo:O atoms is identical in both the prismatic and octahedral columns. This difference in geometry is structurally accommodated by the motion of two oxygen anions by about 1.5 Å, a massive structural rearrangement. As such, it seems likely that any dynamic changes in valence caused by the motion of electrons will necessarily lead to strong changes in local coordination environments, giving rise to exceptionally strong coupling between the lattice and electronic degrees of freedom in this compound and likely leading to polaron formation. It is therefore expected that the disproportionated state cannot easily be disrupted, and physical properties measurements (discussed next) show no evidence for transitions out of the disproportionated state up to the maximum temperature studied (300 °C).

It is of great interest to understand both the crystal chemical forces that permit the stabilization of the mixed valence structure of La_2MoO_5 and the manner in which the mixed valence ions will influence the electronic structure of this compound as well as the dependent physical properties, such as resistivity, magnetic susceptibility, and optical absorption. Magnetic susceptibility measurements generally provide a robust method of probing the number of unpaired electrons at transition-metal sites. The measured magnetic susceptibility (Figure 4) is essentially temperature independent and indicates that La_2MoO_5 should be considered to be diamagnetic. There is a very weak paramagnetic signal which is about 50 times weaker than that expected for a single unpaired electron ($S = 1/2$) which obeys the Curie law and is therefore tentatively attributed to contributions from a minor impurity phase. When explicitly fit to a Curie−Weiss law of the form $\chi = \chi_0 + C/(T - \Theta)$, the refined value for the temperature independent susceptibility χ_0 is 1.3×10^{-5} emu/mol, the Curie constant C is 1.18×10^{-2} emu/(mol K), and the Curie−Weiss Θ is −7.4 K, supporting this assignment. As shown in Figure 4, this diamagnetism is very different from the expectations for a d^1 cation in octahedral coordination ($S = 1/2$) or for a d^3 ion in square planar coordination ($S = 1/2$) and indicates that the direct metal−metal bonding must strongly impact the electronic structure of La_2MoO_5 and provide a mechanism for pairing all of the valence electrons.

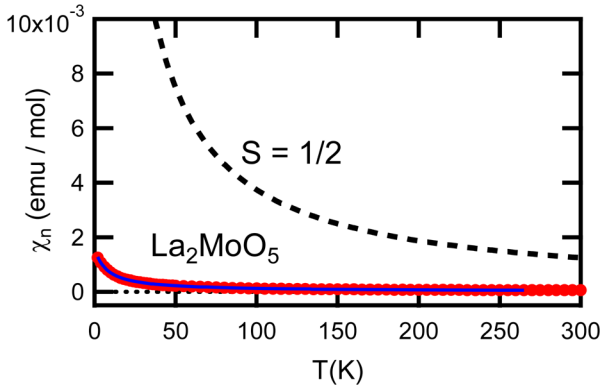

Figure 4. Magnetic susceptibility of La_2MoO_5 (red points) obtained in field cooled measurements with $B = 5$ T is much less than expected for an $S = 1/2$ ion (dashed line) and indicates this phase is diamagnetic. Fits to the small temperature-dependent susceptibility (blue line) are characteristic of a small amount of a paramagnetic impurity.

Temperature-dependent resistivity measurements (Figure 5) indicate that La_2MoO_5 is nonmetallic with a large resistivity of

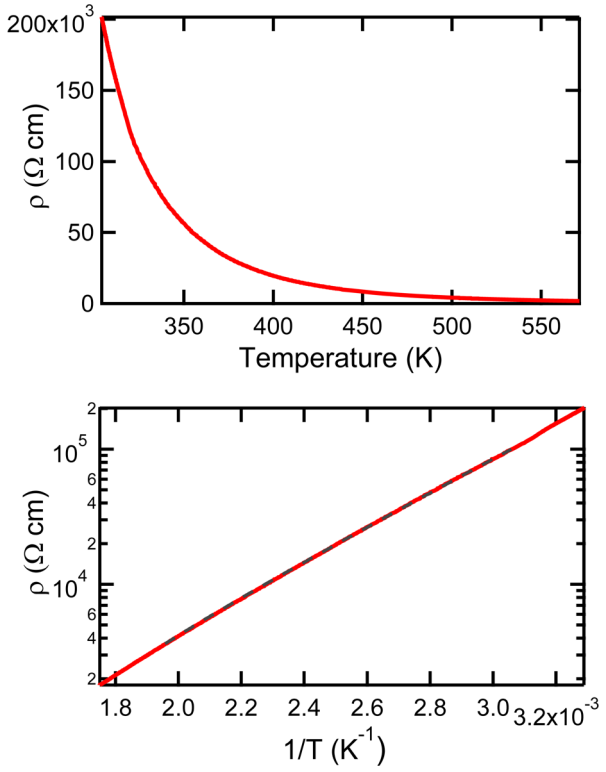

Figure 5. Resistivity of La_2MoO_5 decreases exponentially with increasing temperature, as seen in plots against linear axes (top) and in plots rescaled to be linear when this dependence is followed (bottom). A bandgap of 0.49 eV is obtained from fits to this data (dashed black line).

2.0×10^5 Ω cm at room temperature that drops by 2 orders of magnitude on heating to 300 °C. This behavior is consistent with the magnetic susceptibility data, as the complete pairing of electrons generally precludes the observation of metallic behavior. The temperature dependence exhibits Arrhenius behavior and corresponds to a band gap of 0.49 eV if this

DOI: 10.1021/ja511218g
J. Am. Chem. Soc. 2015, 137, 1245−1257

compound is behaving as a conventional thermally activated semiconductor following the relationship $\rho = \rho_0 e^{-E_g/2kT}$ or a simple thermal gap of 1.0 eV for an alternate type of thermally activated process such as polaronic hopping which is a strong possibility given the very large lattice distortions (oxygen displacement) that accompany the charge disproportionation in this compound.

It is very unusual to find small band gaps in diamagnetic oxide semiconductors. For example, the band gaps of the thermodynamically stable compounds of MoO_3 (2.93 eV), Fe_2O_3 (2.2 eV), TiO_2 (3.0 eV), and Cu_2O (2.0 eV) are all much larger. The wide band gaps of oxide semiconductors are typically due to the substantial electronegativity difference between oxygen and the cation, though the energy scales associated with alternate mechanisms for band gap formation in oxide semiconductors without closed shells (ligand field splitting and/or electronic correlations) also tend to be large. The industrially important small gap semiconductors used for infrared detectors, such as InGaAs,[71] PbS,[72] and InSb,[73] incorporate later p-block anions that are typically susceptible to oxidation in air and often have high toxicity.[74] The availability of small band gap oxide semiconductors for infrared applications may therefore offer many advantages over existing p-block semiconductor systems.

The absorption properties of La_2MoO_5 were directly evaluated using diffuse reflectance data, which were measured over the energy range of 0.5 to 5 eV (Figure 6). It is difficult to resolve the band gap of La_2MoO_5 from the present data, but it appears likely that it falls between 0.4 and 0.7 eV. While it is nontrivial to obtain absolute absorption coefficients, it is expected based on a comparison with other oxide semiconductors measured in the same instrument that the absolute absorption between 0.75−1.00 eV is strong and that this phase will have a good cross-section for the absorption of infrared light in this energy range. Unlike conventional oxide semiconductors whose spectra typically exhibit only one or two features associated with absorption across a direct or indirect gap, the absorbance spectra of La_2MoO_5 exhibit many overlapping optical features which cannot be easily resolved. These features cannot be trivially interpreted, and a deeper understanding of the influence of metal−metal bonding on the electronic structure of La_2MoO_5 is therefore required to understand this data.

Initial insights into electronic structure were obtained through calculations using the LMTO47c code, which is very effective for obtaining insights into the orbital contributions, but which less robust for the determination of band gaps relative to more conventional plane wave codes. The density of states (DOS) and band structure obtained in this manner are plotted in Figures 7 and 8. The dense manifold of orbitals found at energies below −2 eV (relative to the top of the valence band) is assigned to the O 2p states that typically make up the valence band of oxide semiconductors but which do not serve this role in La_2MoO_5. Both the valence and conduction bands are comprised of Mo 4d states, which are the primary contributor to the active bands between −2 and +4 eV. These

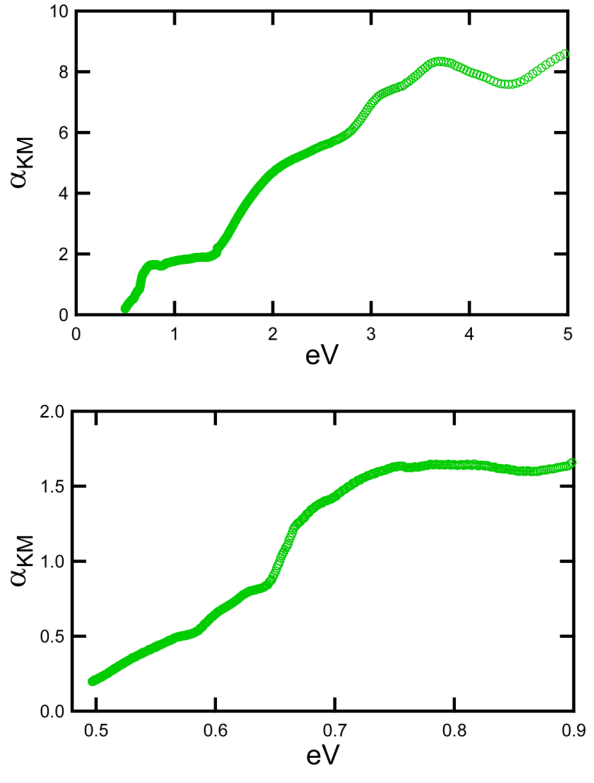

Figure 6. Relative absorbance spectra of La_2MoO_5 obtained from a Kubelka−Munk transform of diffuse reflectance data (top) and with an expanded view of the low-energy infrared response (bottom).

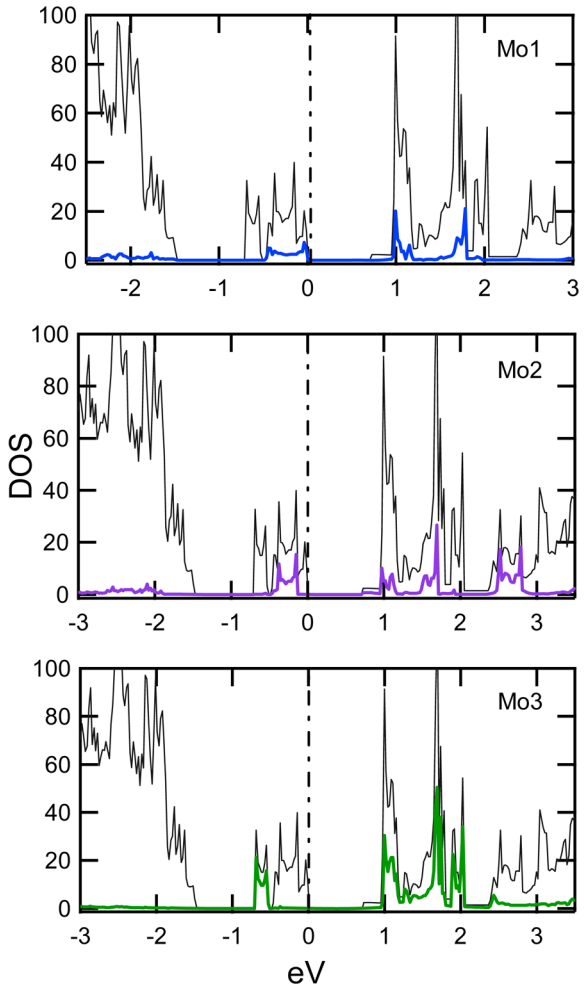

Figure 7. Total (black) and Mo d orbital site-specific (blue/purple/green) DOS for La_2MoO_5.

DOI: 10.1021/ja511218g
J. Am. Chem. Soc. 2015, 137, 1245−1257

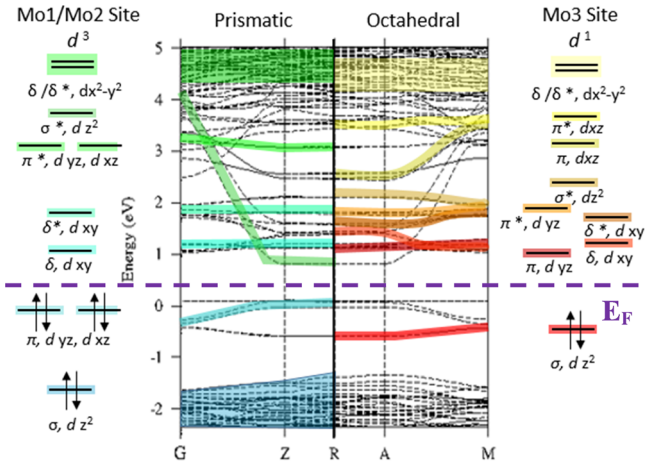

Figure 8. LMTO-calculated band structure of La_2MoO_5 showing a band gap of 0.69 eV between the valence and conduction bands. The orbital splitting diagrams were assigned based on "fatbands" plots, provided in the Supporting Information.

d-electron bands are essentially flat in most reciprocal space directions but are sometimes strongly dispersed in the *z*-axis direction (e.g., G → Z, A → M), likely reflecting the *c*-axis alignment of the polyhedral chains and the Mo−Mo bonds. The lack of dispersion in other directions leads to some very sharp peaks in the DOS associated with the Mo d-electrons, which approach the high DOS values observed for f-electron states. It might therefore be expected that the valence electrons in La_2MoO_5 do not behave like typical d-electrons and may exhibit phenomena such as heavy Fermion behavior that are only commonly observed for f-electron systems. The band gap obtained through these calculations is 0.69 eV, a value which is consistent with the optical measurements, and which is far smaller than typical oxide semiconductors.

An examination of the integrated density of states (IDOS) fully confirms the valence assigned from BVS methods, as the octahedral site (Mo3) is found to have a d^1 configuration, while the prismatic sites (Mo1 and Mo2) both have a d^3 configuration (Figure 8). The prismatic Mo1 and Mo2 sites have similar but not identical electronic states, reflecting the symmetry breaking that occurs in this $\sqrt{2} \times \sqrt{2}$ superstructure. Based on these calculations, the Mo−Mo bonds in Mo_2O_8 can be assigned a bond order of three (triple bond) and those of the Mo_2O_{10} octahedral dimers a bond order of one (single bond).

In order to assign the orbital character of the occupied and unoccupied d-electron states, "fatbands" calculations were carried out. A condensed description of these results is provided in Figure 8, while the full analysis (five individual sets of fatbands for each of the three types of Mo sites) is given in Figures S3−S6. In general, it can be seen that each type of dimeric Mo site gives rise to more than five d-orbital states. This indicates that a single-ion analysis is incomplete and that the 10 combined molecular orbitals that can be derived from the d-orbitals on a pair of Mo cations must be considered.

The Mo_2O_{10} dimers are built from Mo cations on the Mo3 site. Although these Mo3 cations can be assigned a d^1 configuration based on their oxidation state, they do not have one single unpaired d-electron residing in the lowest energy d-orbital of the t_{2g} manifold as would typically be expected for an isolated MoO_6 octahedron in the single-ion picture. Instead, the lowest energy t_{2g} orbital (with d_{z^2} symmetry, when described using the nonstandard axis choices most relevant to the dimer shown in Figure 3) for the Mo3 site is split into a separate bonding and antibonding pairs when the two orbitals of this symmetry (one for each Mo3 in the dimer) are allowed to hybridize. The lower energy bonding orbital contains two paired electrons (one electron from each Mo3 site in the Mo_2O_{10} dimer) and will therefore have a closed shell. Similarly, the higher energy antibonding orbital is completely empty and will also be diamagnetic in character. These bonding and antibonding orbitals are given the labels σ and σ^*, using the standard chemistry terminology to describe the direct overlap of their lobes. The 10 d-orbitals associated with the Mo_2O_{10} and Mo_2O_8 dimers can therefore be assigned both single-ion labels (d_{xy}, d_{yz}, d_{zx}, $d_{x^2-y^2}$, d_{z^2}) and molecular orbital labels (σ, σ^*, π, π^*, δ, δ^*), which are marked in Figure 9. The relative

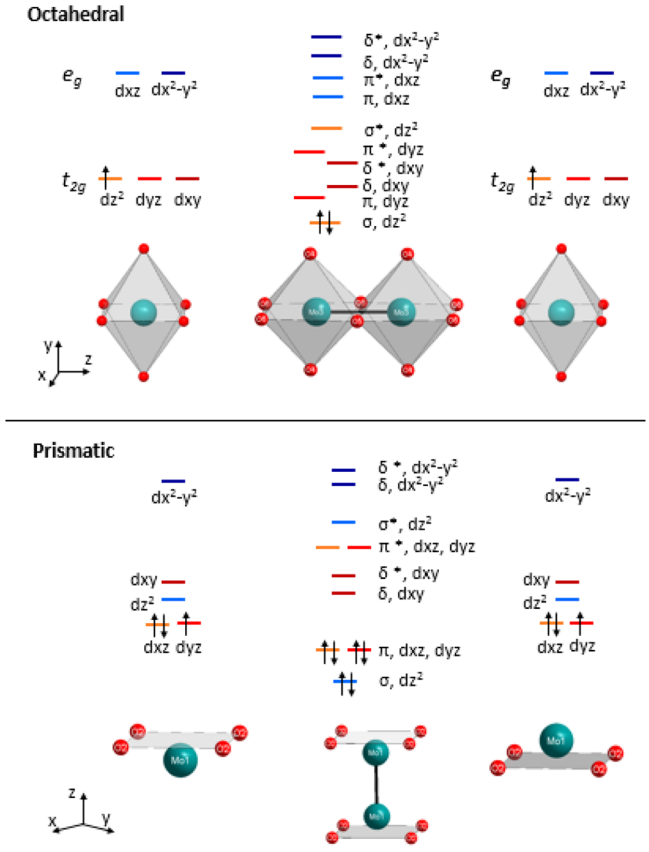

Figure 9. Molecular orbital ordering diagram for the d electrons involved in forming the metal−metal bond for both the Mo_2O_{10} and Mo_2O_8 dimer types.

energies of these orbitals can be clearly enumerated in most cases, though for highly dispersed orbitals, the midpoint energy of the orbital is an inadequate descriptor of the wide range of energies at which the orbital contributes to the overall DOS.

Although predictions about the physical properties of La_2MoO_5 made using only the single-ion picture are clearly inaccurate, the single-ion model still provides a good starting point for estimating the energies of the molecular orbitals (MOs), and these MOs are very effective for describing the electronic properties of this phase. For example, in the single ion picture for the Mo3 site, an octahedral ion with the nonstandard choice of reference axes given in Figure 9 will be split into lower energy triply degenerate t_{2g} (d_{z^2}, d_{yz}, d_{xy}) and

DOI: 10.1021/ja511218g
J. Am. Chem. Soc. 2015, 137, 1245−1257

higher energy double degenerate e_g ($d_{x^2-y^2}$, d_{xz}) states. The higher energies of the e_g orbitals result from the stronger repulsive interactions with the ligand electrons for the d-orbitals which have lobes oriented toward those ligands, and it is sensible that these repulsions persist even after the d-orbitals from two different Mo cations hybridize to form MOs. The molecular orbitals observed for La_2MoO_5 maintain the same general arrangement, as the 6 MOs (σ, σ^*, π, π^*, δ, δ^*) derived from t_{2g} states are substantially lower in energy than the 4 MOs (π, π^*, δ, δ^*) derived from e_g states. The hybridization that results from the metal−metal bonding will result in each single-ion d-orbital being split into bonding and antibonding pairs, with the σ orbitals (d_{z^2}) having a very large splitting, the π orbitals (d_{xz}, d_{yz}) having a smaller but still very substantial splitting, and the δ orbitals (d_{xy}, $d_{x^2-y^2}$) having minimal splitting. When these two primary factors (relative energies of single ion orbitals and the relative degree of hybridization for molecular orbitals) are considered together, accurate predictions can be made about the relative energies and splitting of the 10 d-orbital-derived MOs associated with the Mo_2O_{10} dimers.

A similar analysis can be made for the square prismatic Mo_2O_8 dimers. The two types of dimers (with Mo1 and Mo2 sites) have nearly identical local environments, and thus the splitting of the Mo d orbitals occurs in the same manner for these two sites. The starting point for understanding the Mo_2O_8 energy levels is the single ion picture, and each Mo cation resides in what is effectively a square planar environment. The relative energies of the 5 d-orbitals in the square prismatic ligand field environment can be understood by thinking of the prisms as octahedra in which the repulsive interactions in the z-axis direction have been removed due to the lack of axial ligands in this direction, resulting in d-orbitals being stabilized (moving to lower energy) in proportion to their z-axis component. Thus, the d_{z^2} orbital is strongly stabilized, the d_{xz} and d_{yz} orbitals are modestly stabilized, and the d_{xy} and $d_{x^2-y^2}$ orbital energies are essentially unchanged relative to an ideal octahedron with the difference in their relative energies remaining that of the octahedral crystal field splitting, Δ_O (as shown in Figure S7). Since the prismatic sites have four-fold rotational symmetry along their z-axis, the d_{xz} and d_{yz} orbitals are necessarily identical in energy and are completely degenerate in the single-ion picture.

The π and π^* MOs derived from the d_{xz} and d_{yz} orbitals do not break the four-fold symmetry and thus preserve this degeneracy of their parent orbitals. As a result, the d-orbital states associated with the Mo_2O_8 dimers will form MOs with 8 different energies, in contrast to the 10 nondegenerate MOs that form for the Mo_2O_{10} bioctahedra. Although the d_{z^2} orbital has only the third-lowest energy in the single-ion picture, the σ-bonding MO derived from this orbital will have the lowest energy among the MOs associated with the Mo_2O_8 dimers and will be fully occupied. The other two fully occupied MOs will be the degenerate π-bonding orbitals derived from the d_{xz} and d_{yz} single-ion orbitals, which have both the lowest energy in the single ion picture and the second-highest degree of hybridization in the presence of metal−metal bonding. The lowest unoccupied molecular orbital (LUMO) is expected to be the δ-bonding orbital derived from the single-ion d_{xy} orbital, followed by the δ^*, π^*, and σ^* antibonding orbitals at somewhat higher energies, and the δ and δ^* orbitals derived from the $d_{x^2-y^2}$ orbital at much higher energy.

The initial orbital assignments obtained using simpler LMTO methods on unrelaxed structures were confirmed when further LDA and LDA+U calculations using the projector augmented wave method that incorporated internal structural relaxation were carried out. The band gaps obtained using LDA (indirect 0.50, eV; direct, 0.64 eV) and LDA+U (indirect 0.68, eV; direct, 0.81 eV) are roughly consistent with both the LMTO result and the experimental onset of absorption. The LDA+U results were then used to directly calculate the optical response expected for La_2MoO_5 (Figure 10) in order to better understand the manner in which metal−metal bonding affects the optical response of this compound.

This optical response is nontrivial to interpret since Mo ions are found in three spatially distinct crystallographic sites with

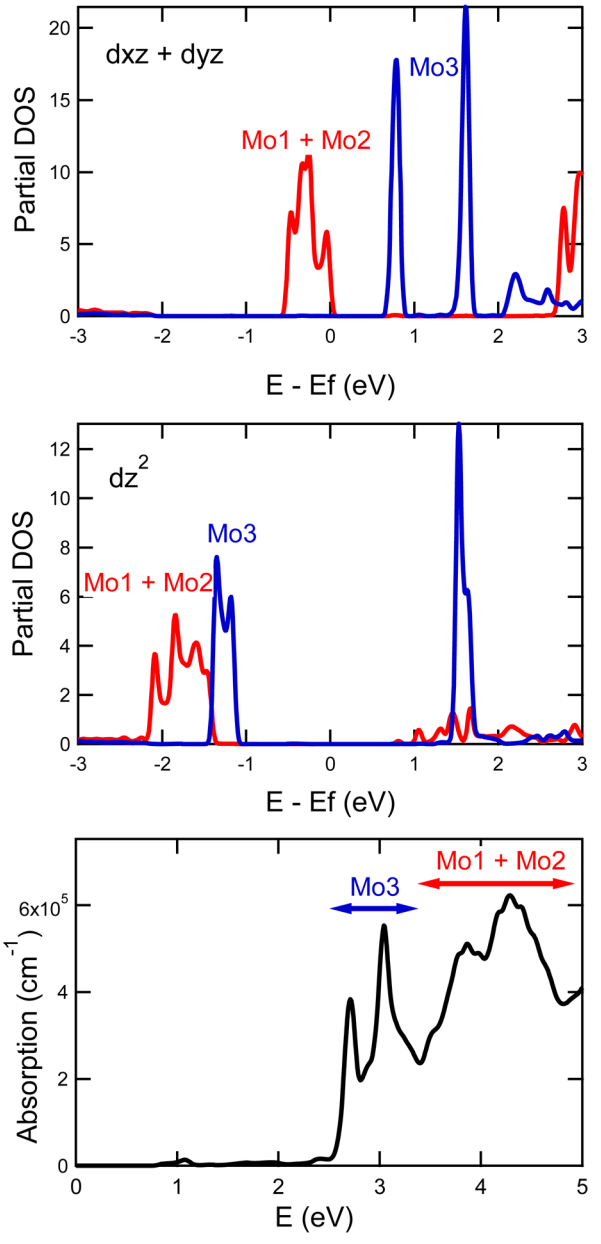

Figure 10. Top: Projected d_{xz} and d_{yz} DOS for the prismatic Mo1 and Mo2 sites (red) and for the octahedral Mo3 sites (blue). Center: Projected d_{z^2} states. Bottom: Calculated (LDA+U) absorption cross section including contributions from direct, dipole allowed transitions. While most d−d excitations are predicted to be very weak, strong σ−σ^* transitions of the octahedral d_{z^2} states are clearly seen for photon energies of 2.5−3.5 eV.

DOI: 10.1021/ja511218g
J. Am. Chem. Soc. 2015, 137, 1245−1257

two different types of local coordination geometries. An analysis of the LDA+U results finds that the highest occupied states are mainly on the prismatic Mo1 and Mo2 sites (d_{xz} and d_{yz} π-bonding states), while the lowest unoccupied states of minimal energy are associated with a number of different orbital states with π and δ character on all three types of Mo sites. As a result, all of the possible optically induced transitions among these frontier orbitals involve weakly overlapping d-electron states with π and δ character. This is reflected in the weak optical response due to dipole allowed transitions calculated for energies below 2.5 eV.

Around 2.5 eV, calculations predict the onset of an intense response originating from strongly coupled σ and σ^* states associated with the octahedral dimers of the Mo3 site. A similarly intense response is also seen for the Mo1 and Mo2 sites, though with a higher onset energy of ∼3.5 eV that likely reflects the stronger hybridization associated with the much shorter bond length of the prismatic dimers. This intense $\sigma-\sigma^*$ excitation occurs for d_{z^2} orbitals aligned along the axis of the Mo−Mo bond in the dimers and presumably reflects the fact that this specific transition is no longer symmetry forbidden when the ideal symmetry of each component MoO_6 octahedra is strongly broken in this direction due to the anisotropy induced by dimerization. The optical response associated with this $\sigma-\sigma^*$ excitation is essentially fully polarized in the z-axis direction (Figure S8), reflecting the nature of the orbital contributions.

The fact that the calculated LDA+U optical response (Figure 10) appears very different from the experimentally measured optical response (Figure 6) can also be ascribed to symmetry breaking effects. The LDA+U calculations suggest a very weak absorption at low energies followed by an abrupt onset of strong absorption around 2.5 eV, in contrast to the experimental data which show a roughly linear increase in the intensity of absorption from the band gap up to the upper limit of the measurements (∼5 eV). The DFT calculations were done for a frozen lattice with no account of vibrations, conditions under which the coordination polyhedra should have a reasonably ideal geometry based on the bond lengths (Table 4) determined from the average atomic positions (Table 3). The experimental optical data were collected at room temperature, and the mean displacements for Mo and O ions are expected to be about 0.08−0.11 Å at this temperature based on estimates from the relationship $B_{eq} = 8\pi^2\langle u^2\rangle$. The thermal vibrations of these ions are therefore expected to cause very substantial distortions of the local symmetry, and optical transitions which are symmetry forbidden at low temperature should become much more allowed at room temperature. It is therefore anticipated that agreement between theoretical predictions and experimental observations would substantially improve if DFT calculations were carried out for trial structures with thermal displacements of ∼0.1 Å or if the 0 K DFT results were instead compared to optical data collected at cryogenic temperatures for which phonons and their accompanying thermal displacements are effectively suppressed.

One curious aspect of the experimentally determined La_2MoO_5 structure is the substantially different refined Mo−Mo bond lengths for the Mo1 site (2.22 Å) and the Mo2 site (2.28 Å), both of which have prismatic local environments that are equivalent and identical in the parent La_2ReO_5 structure type. These two Mo−Mo bond lengths have unusually large estimated standard deviation of ∼0.02 Å that are about 4 times larger than those of the Mo−O or La−O bonds, and which can be confirmed to reflect strong correlations in the refined positions of these two distinct Mo sites by an examination of the correlation matrix of the structure refinement. It is therefore unclear if these differences in bond length are real or reflect an artifact of the refinement. This quandary was addressed through further LDA calculations in which full structure relaxation was carried out by fitting the volume dependence of total energy to the Murnaghan equation of state (Figure S9). The equilibrium lattice parameters obtained in this manner were about 1.5% smaller than then experimentally determined values, as is typically observed for LDA calculations for compounds which do not exhibit strong correlation effects. The Mo−Mo bond lengths calculated for the fully relaxed DFT structure are 2.21, 2.25, and 2.62 Å for the Mo1, Mo2, and Mo3 sites, respectively. The experimental conclusion of a shorter bonds at the Mo1 site than at the Mo2 site is therefore supported by theory and likely occurs as a result of the slightly different alignment of the two prismatic sites relative to the octahedral chains that occur at the Mo3 site. The different alignments are made possible by the reduction in symmetry of the octahedral Mo3 sites (two-fold) relative to the four-fold symmetry found in the exclusively square prismatic sites in the parent La_2ReO_5 structure.

CONCLUSIONS

It is demonstrated that the novel structure of La_2MoO_5 corresponds to a superstructure of the parent La_2ReO_5 structure in which charge disproportionation occurs, leading to equal amounts of Mo^{5+} ions occurring in Mo_2O_8 square prismatic dimers and Mo^{3+} ions occurring in Mo_2O_{10} octahedral dimers. This is the first example Mo charge disproportionation observed in a solid-state compound. The presence of direct metal−metal bonding in these dimers lifts the d-orbital degeneracy for the Mo cations in the dimers, resulting in 8 different sets of orbital states for the Mo_2O_8 prisms and 10 for the Mo_2O_{10} dimers. Through bond valence sum calculations it is shown that the presence of Mo−Mo bonding results in the weakening of Mo−O bonds. Although the electronic structure associated with La_2MoO_5 is complex, it is demonstrated that its main features can be readily explained within a molecular orbital picture in which the energy states expected for a single-ion configuration hybridize to form bonding (σ, π, δ) and antibonding (σ^*, π^*, δ^*) states which are roughly centered about the single-ion levels from which they are derived. This hybridization causes La_2MoO_5 to become a small band gap semiconductor which has very substantial infrared absorption at room temperature, unlike the vast majority of oxide compounds. The structure−property relationships developed here provide a general framework for interpreting the complex behavior of compounds with metal−metal bonding and for predictively harnessing the unusual electronic states of these oxide materials for technological applications.

ASSOCIATED CONTENT

Supporting Information

Rietveld refinement results, tabulation of BVS calculations, detailed fatband analysis of band structure, and Murgnaghan equation of state fit. This material is available free of charge via the Internet at http://pubs.acs.org.

AUTHOR INFORMATION

Corresponding Author

*Peter.Khalifah@stonybrook.edu

DOI: 10.1021/ja511218g
J. Am. Chem. Soc. 2015, 137, 1245−1257

Notes

The authors declare no competing financial interest.

■ ACKNOWLEDGMENTS

This work was supported by the National Science Foundation grant no. DMR-0955646. The portion of this research conducted at Oak Ridge National Laboratory's Spallation Neutron Source was sponsored by the Scientific User Facilities Division, Office of Basic Energy Sciences, U.S. Department of Energy. This research used resources of the Advanced Photon Source, a U.S. Department of Energy (DOE) Office of Science User Facility operated for the DOE Office of Science by Argonne National Laboratory under contract no. DE-AC02-06CH11357. Research was carried out in part at the Center for Functional Nanomaterials, Brookhaven National Laboratory, which is supported by the U.S. Department of Energy, Office of basic Energy Sciences, under contract no. DE-AC02-98CH10886.

■ REFERENCES

(1) Rao, C. *Annu. Rev. Phys. Chem.* **1989**, *40*, 291.
(2) Griffith, J.; Orgel, L. *Q. Rev. Chem. Soc.* **1957**, *11*, 381.
(3) Gautier, R.; Andersen, O.; Gougeon, P.; Halet, J.; Canadell, E.; Martin, J. *Inorg. Chem.* **2002**, *41*, 4689.
(4) Xu, J.; Sonne, M.; Pryds, N.; Kleinke, H. *J. Alloys Compd.* **2010**, *489*, 353.
(5) Gougeon, P.; Gall, P.; Halet, J.; Gautier, R. *Acta Crystallogr. B* **2003**, *B59*, 472.
(6) Wilhelmi, K.; Lagervall, E.; Muller, O. *Acta Chem. Scand.* **1970**, *24*, 3406−3408.
(7) Sasaki, A.; Wakeshima, M.; Hinatsu, Y. *J. Phys.: Condens. Matter* **2006**, *18*, 9031.
(8) Khalifah, P.; Nelson, K.; Jin, R.; Mao, Z.; Liu, Y.; Huang, Q.; Gao, X.; Ramirez, A.; Cava, R. *Nature* **2001**, *411*, 669.
(9) Khalifah, P.; Cava, R. *Phys. Rev. B* **2001**, *64*, 085111.
(10) Kreisel, K.; Yap, G.; Dmitrenko, O.; Landis, C.; Theopold, K. *J. Am. Chem. Soc.* **2007**, *129*, 14162.
(11) Cotton, F. *Acc. Chem. Res.* **1969**, *2*, 240.
(12) Nguyen, T.; Sutton, A.; Brynda, M.; Fettinger, J.; Long, G.; Power, P. *Science* **2005**, *310*, 844.
(13) Gall, P.; Gougeon, P. *Acta Crystallogr. C* **1992**, *48*, 1915.
(14) Torardi, C.; Fecketter, C.; McCarroll, W.; DiSalvo, F. *J. Solid State Chem.* **1985**, *60*, 332.
(15) Ledesert, M.; Labbe, P.; McCarroll, W.; Leligny, H.; Raveau, B. *J. Solid State Chem.* **1993**, *105*, 143.
(16) Moini, A.; Subramanian, M.; Clearfield, A.; DiSalvo, F.; McCarroll, W. *J. Solid State Chem.* **1987**, *66*, 136.
(17) Cuthbert, H.; Greedan, J.; Vargas-Baca, I.; Derakhshan, S.; Swainson, I. *Inorg. Chem.* **2007**, *46*, 8739.
(18) Besse, J.; Baud, G.; Chevalier, R. *Acta Crystallogr. B* **1978**, *B34*, 3532.
(19) Jeitschko, W.; Heumannskamper, D.; Rodewald, U.; Schriewer-Pottgen, M. *Z. Anorg. Allg. Chem.* **2000**, *626*, 80.
(20) Sleight, A. L.; JM. *Inorg. Chem.* **1968**, *7*, 108.
(21) Wlschek, G.; Paulus, H.; Ehrenberg, H.; Fuess, H. *J. Solid State Chem.* **1997**, *132*, 196.
(22) Waltersson, K. *Acta Crystallogr. B* **1976**, *32*, 1485.
(23) Jeitschko, W.; Heumannskamper, D.; Schriewer-Pottgen, M.; Rodewald, U. *J. Solid State Chem.* **1999**, *147*, 218−228.
(24) Gall, P.; Barrier, N.; Gautier, R.; Gougeon, P. *Inorg. Chem.* **2002**, *41*, 2879.
(25) Gall, P.; Gautier, R.; Halet, J.; Gougeon, P. *Inorg. Chem.* **1999**, *38*, 4455.
(26) Xue, J.; Antonio, M.; Soderholm, L. *Chem. Mater.* **1995**, *7*, 333.
(27) Muller, O.; Roy, R. *Mater. Res. Bull.* **1969**, *4*, 349.
(28) Kerner-Czeskleba, H.; Tourne, G. *Mater. Res. Bull.* **1978**, *13*, 271.
(29) Hubert, P.; Laffitte, M. *C. R. Seances Acad. Sci., Ser. C* **1977**, *285*, 567.
(30) Manthiram, A.; Gopalakrishnan, J. *J. Less-Common Met.* **1979**, *68*, 167.
(31) Manthiram, A.; Gopalakrishnan, J. *P. Indian Acad. Sci.* **1978**, *8*, 267.
(32) Lagervall, E.; Lofgren, P.; Waltersson, K.; Wilhelmi, K. *Acta Crystallogr. A* **1975**, *31*, S88.
(33) Shi, F.; Meng, J.; Ren, Y. *Solid State Commun.* **1995**, *95*, 745.
(34) McCarroll, W.; Darling, C.; Jakubicki, G. *J. Solid State Chem.* **1983**, *48*, 189.
(35) Andersen, O.; Pawlowska, Z.; Jepsen, O. *Phys. Rev. B* **1986**, *34*, 5253.
(36) Blochl, P. *Phys. Rev. B* **1994**, *50*, 17953.
(37) Kresse, G.; Joubert, D. *Phys. Rev. B* **1999**, *59*, 1758.
(38) Kresse, G.; Furthmuller, J. *Phys. Rev. B* **1996**, *54*, 11169.
(39) Ceperley, D.; Alder, B. *Phys. Rev. Lett.* **1980**, *45*, 566.
(40) Perdew, J.; Zunger, A. *Phys. Rev. B* **1981**, *23*, 5048.
(41) Dudarev, S.; Botton, G.; Savrasov, S.; CJ, H.; Sutton, A. *Phys. Rev. B* **1998**, *57*, 1505.
(42) Vaugier, L.; Jiang, H.; Biermann, S. *Phys. Rev. B* **2012**, *86*, 165105.
(43) Murnaghan, F. *P. Natl. Acad. Sci. USA* **1944**, *30*, 244.
(44) Oszlanyi, G.; Sueto, A. *Acta Crystallogr. A* **2004**, *60*, 134.
(45) Pearson, R. *J. Mol. Struct.* **1983**, *103*, 25.
(46) Brese, N.; O'Keeffe, M. *Acta Crystallogr. B* **1991**, *B47*, 192.
(47) Chen, M.; Zhou, Z.; Hu, S. *Chin. Sci. Bull.* **2002**, *47*, 978.
(48) Brown, I.; Altermatt, D. *Acta Crystallogr. B* **1985**, *B41*, 244.
(49) Sleight, A. W. *Prog. Solid State Chem.* **2009**, *37*, 251.
(50) Robin, M. B.; Day, P. In *Advances in Inorganic Chemistry and Radiochemistry*; Emeléus, H. J., Sharpe, A. G., Eds.; Academic Press: New York, 1968; Vol. *10*, p 247.
(51) Pickett, W.; Quan, Y.; Pardo, V. *J. Phys.: Condens. Matter* **2014**, *26*, 274203.
(52) Orosel, D.; Balog, P.; Liu, H.; Qian, J.; Jansen, M. *J. Solid State Chem.* **2005**, *178*, 2602.
(53) Sleight, A. W.; Gillson, J. L.; Bierstedt, P. E. *Solid State. Commun.* **1975**, *17*, 27.
(54) Cava, R. J.; Batlogg, B.; Krajewski, J. J.; Farrow, R.; Rupp, L. W.; White, A. E.; Short, K.; Peck, W. F.; Kometani, T. *Nature* **1988**, *332*, 814.
(55) Cava, R. J.; Batlogg, B.; Espinosa, G. P.; Ramirez, A. P.; Krajewski, J. J.; Peck, W. F.; Rupp, L. W.; Cooper, A. S. *Nature* **1989**, *339*, 291.
(56) Retuerto, M.; Emge, T.; Hadermann, J.; Stephens, P.; Li, M.; Yin, Z.; Croft, M.; Ignatov, A.; Zhang, S.; Yuan, Z.; Jin, C.; Simonson, J.; Aronson, M.; Pan, A.; Basov, D.; Kotliar, G.; Greenblatt, M. *Chem. Mater.* **2013**, *25*, 4071.
(57) Kotliar, G.; Yin, Z. *EPL* **2013**, *101*, 27002.
(58) Woodward, P.; Cox, D.; Moshoppoulou, E.; Sleight, A.; Morimoto, S. *Phys. Rev. B* **2000**, *62*, 844.
(59) Huynh, M.; Bediako, D.; Nocera, D. *J. Am. Chem. Soc.* **2014**, *136*, 6002.
(60) Zaghrioui, M.; Bulou, A.; Lacorre, P.; Laffez, P. *Phys. Rev. B* **2001**, *64*, 081102.
(61) Zhao, Q.; Darriet, J.; Whangbo, M.; Ye, L.; Stackhouse, C.; zurLoye, H. *J. Am. Chem. Soc.* **2011**, *133*, 20981.
(62) Kojima, N. *B. Chem. Soc. Jpn.* **2000**, *73*, 1445.
(63) Bland, S.; Angst, M.; Adiga, S.; Scagnoli, V.; Johnson, R.; Herrero-Martin, J.; Hatton, P. *Phys. Rev. B* 2010, *82*.
(64) Akrap, A.; Angst, M.; Khalifah, P.; Mandrus, D.; Sales, B.; Forro, L. *Phys. Rev. B* **2010**, *82*, 165106.
(65) Attfield, J.; Bell, A.; Rodriguez-Martinez, L.; Greneche, J.; Cernik, R.; Clarke, J.; Perkins, D. *Nature* **1998**, *396*, 655.
(66) Radaelli, P. G.; Horibe, Y.; Gutmann, M. J.; Ishibashi, H.; Chen, C. H.; Ibberson, R. M.; Koyama, Y.; Hor, Y.-S.; Kiryukhin, V.; Cheong, S.-W. *Nature* **2002**, *416*, 155.
(67) Takubo, K.; Hirata, S.; Son, J.; Quilty, J.; Mizokawa, T.; Matsumoto, N.; Nagata, S. *Phys. Rev. Lett.* **2005**, *95*, 246401.

DOI: 10.1021/ja511218g
J. Am. Chem. Soc. 2015, 137, 1245−1257

(68) Verwey, E. *Nature* **1939**, *144*, 327.
(69) Senn, M. S.; Wright, J. P.; Attfield, J. P. *Nature* **2012**, *481*, 173.
(70) Goff, R.; Wright, J.; Attfield, J.; Radaelli, P. G. *J. Phys.: Condens. Matter* **2005**, *17*, 7633.
(71) Yuan, Z. K. B.; Sharpe, A.; Shields, A. *Appl. Phys. Lett.* 2007, *91*.
(72) Hines, M.; Scholes, G. *Adv. Mater.* **2003**, *15*, 1844.
(73) Phelan, R.; Calawa, A.; Rediker, R.; Keyes, R.; Lax, B. *Appl. Phys. Lett.* **1963**, *3*, 143.
(74) Rogalski, A. *Prog. Quant. Electron.* **2003**, *27*, 59.

DOI: 10.1021/ja511218g
J. Am. Chem. Soc. 2015, 137, 1245−1257